SAND2007-8049C
08PFL-740

Large Eddy Simulation of Direct Injection Processes for Hydrogen and LTC Engine Applications

Tomasz G. Drozda and Joseph C. Oefelein
Sandia National Laboratories, Livermore, CA

ABSTRACT

Direct injection (DI) has proven to be a promising option in Diesel and low temperature combustion engines. In conventional Diesel and homogeneous charge compression ignition (HCCI) applications, DI lowers soot and NO_x production and improves fuel economy. In hydrogen fueled engines, DI provides the appropriate energy density required for high efficiency and low NO_x emissions. To realize the full benefit of DI, however, the effect of various injection parameters, such as injection timing, duration, pressure, and dilution, must be investigated and optimized under a range of engine operating conditions. In this work, we have developed a model for high-fidelity calculations of DI processes using the Large Eddy Simulation (LES) technique and an advanced property evaluation scheme. Calculations were performed using an idealized domain to establish a baseline level of validation. The theoretical-numerical framework combines a general treatment of the governing conservation and state equations with state-of-the-art numerical algorithms and massively-parallel programming paradigms. This software enables both the canonical cases described here and in-cylinder calculations. Here we focus on high-pressure multi-port gas injectors designed for application in hydrogen-fueled IC-engines. This study was conducted in support of a larger effort to perform detailed in-cylinder LES calculations of companion optical engine experiments.

INTRODUCTION

Direct injection (DI) has proven to be of great importance for controlling combustion processes in internal combustion engines (ICE's). In Diesel engines, injected liquid fuel atomizes and evaporates while undergoing turbulent mixing with the oxidizer. These physical interactions, and in particular the level of mixing, affects the formation of soot and nitrogen oxides (NO_x). Similarly, homogeneous charge compression ignition (HCCI) technology has received much attention due to its high efficiency, low emissions combustion mechanism [1]. HCCI relies on autoignition of lean, or dilute, fuel-oxidizer mixtures at low flame temperatures [2] rather than on the propagation of high temperature flames. The former mode of combustion significantly reduces soot and NO_x production. But, when the equivalence ratio and temperature of the mixture decrease to below 0.15 and 1500K, respectively, combustion efficiency decreases [3]. Direct injection during the intake stroke or early compression stroke has been used as an effective way to control the mixture in a way that provides high efficiency and minimum emissions.

Recent research on hydrogen-fueled ICE's (H_2-ICE's) has demonstrated a potential to operate a transportation power plant with near-zero engine-out emissions [4, 5]. Unlike Diesel engines, H_2-ICE's are spark ignited (SI). The clean operation of the H_2-ICE's is largely due to the low flammability limit of hydrogen. This allows for stable engine operation at highly dilute low temperature conditions, which greatly reduces NO_x emissions. However, other properties of hydrogen make its combustion prone to knock, pre-ignition, and high levels of NO_x production. The later difficulty is mediated by diluting the fuel with EGR and using a three-way catalyst [6]. While spark knock is a property of the fuel, pre-ignition properties depend on the engine design and the control strategy. In early research, the pre-ignition requirements of hydrogen cast doubt on its viability as a fuel. The most promising technique to control pre-ignition and boost power output is DI.

The primary challenge with DI H_2-ICE's is injection timing and enhancement of mixing. Typically, gaseous hydrogen (although cryogenic hydrogen can also be used [6]) is injected at intake valve closure (IVC). While this eliminates

the possibility of backfire, it also sets an upper limit on the mixing time between fuel and oxidizer before the mixture is ignited by the spark. In practice, the mixing time is lowered further by delaying the injection time with respect to IVC to avoid a partially premixed fuel-oxidizer mixture from contacting in-cylinder hot spots and pre-igniting. The start of injection (SOI), therefore, affects the level of unmixedness of the mixture at the time of spark ignition and has a direct impact on pollutant formation [7]. Delaying SOI decreases not only the mixing time, but also the injection duration. Therefore, to realize the full benefit of DI while delivering a sufficient load, a large burden is placed on the injector to supply the fuel at increasingly high pressures and flow rates. Current injector technology limits engine operation from low to medium speeds [8].

To investigate issues related to high-pressure gas injection processes, we have developed a general model framework that combines a detailed property evaluation scheme for arbitrary gas-liquid hydrocarbon mixtures (including hydrogen, oxygen and nitrogen) with the Large Eddy Simulation (LES) technique. In LES, the large energy containing scales of fluid motion are solved on a computational grid. The small (more universal) subgrid-scale (SGS) interactions are modeled. This allows time-accurate predictions of unsteady turbulent flow fields. In contrast, the Reynolds-Averaged Navier-Stokes (RANS) approximation, where both large and small scales of fluid motion are ensemble averaged, only provides a bulk representation of these unsteady dynamics.

LES can be inherently more accurate, albeit more computationally expensive. The mathematical foundations of LES and its applicability in single and multiphase combustion are well established [9–13]. Several researchers have used, both, RANS and LES to perform DI studies [14–17]. As a step toward the systematic validation of our theoretical-numerical framework, we have considered a series of canonical cases with current emphasis placed on high-pressure injectors designed for application in H_2-ICE's. Results are compared to the experimental data acquired by Petersen and Ghandhi [18, 19].

EXPERIMENTAL DATA

High-pressure multi-port hydrogen injector studies were conducted in an optically accessible chamber by Petersen and Ghandhi [18, 19]. Single, three, seven, nine, and thirteen port injectors were used. Single jet injection was achieved by blocking all but the central port of the seven port injector, or realigning one port of the three port injector with the chamber axis. Jet flow patterns were visualized using a Schlieren technique. The images were processed to determine the penetration length and angle. The pressure history during injection was also measured to determine the mass flow rate of the injected gas. Injection pressure, injected gas, chamber density, and chamber gas composition were varied to isolate the effects of pressure, density, compressibility, and ratio of specific heats. A summary of experimental conditions are provided in Tables. 1–3.

Table 1: Injection conditions considered in the experiments of Petersen [19].

Case	p_i† (MPa)	ρ_i‡ (kg/m^3)	Gas§
1	10.4	8.50	H_2
2	10.4	16.1	He
3	7.00	79.1	N_2
4	5.20	4.29	H_2
5	5.20	8.32	He
6	5.20	59.6	N_2
7	8.72		H_2, He
8	6.97		H_2, He
9	3.55		H_2, He
10	1.82		H_2, He
11	0.13–0.38¶		H_2, He

†Injection pressure
‡Injection gas density
§Injection gas composition
¶0.13, 0.15, 0.19, 0.21, 0.24, 0.27, 0.32, 0.35, 0.38

Table 2: Chamber conditions considered in the experiments of Petersen [19].

Case	p_a† (MPa)	ρ_a‡ (kg/m^3)	Gas§
1	0.10	1.15	N_2
2	0.34	3.80	N_2
3	0.46	8.17	CO_2
4	0.72	12.8	CO_2
5	0.72	8.17	N_2

†Ambient chamber pressure
‡Ambient chamber gas density
§Chamber gas composition

Tables 1 and 2 show the range of conditions for the injection process and the chamber, respectively. Table 3 describes which multi-port hydrogen injectors were used in different cases. The numbers in this table denote the number of ports in an injector considered with corresponding injection and chamber conditions. The designations "all" and "none" indicate that all, or none, of the injectors were considered under corresponding injection and chamber conditions. These data were used to establish baseline validation of the model described below.

THEORETICAL–NUMERICAL FRAMEWORK

THEORETICAL FORMULATION. Results presented here were obtained using the theoretical-numerical framework developed by Oefelein [12, 13]. The numerical framework solves the fully coupled conservation equations of mass, momentum, total-energy and species. These equations can be expressed in conservative form as follows:

Table 3: Injector types studied under different injection and chamber conditions.

	Table 2				
Table 1	1	2	3	4	5
1	all†	all	3,7	all	all
2	all	all	7	all	all
3	all	all	none	none	all
4	all	all	3,7	all	all
5	all	all	7	all	all
6	all	all	none	none	all
7	3	3	none	none	3
8	3,7‡	3,7‡	none	none	3,7‡
9	3,7‡	3,7‡	none	none	3,7‡
10	3,7‡	3,7‡	none	none	3,7‡
11	1§	1	none	none	none

†All denotes the 3,7,9,and 13 port injectors

‡H_2 only

§Single jet is achieved by blocking all but the central port of seven port injector, or realigning one port of a three port injector with a chamber axis

- Mass:

$$\frac{\partial \rho}{\partial t} + \nabla \cdot (\rho \mathbf{u}) = 0. \tag{1}$$

- Momentum:

$$\frac{\partial}{\partial t}(\rho \mathbf{u}) + \nabla \cdot \left[\rho \mathbf{u} \otimes \mathbf{u} + \frac{p}{M^2}\mathbf{I}\right] = \nabla \cdot \tau, \tag{2}$$

where

$$\tau = \frac{\mu}{Re}\left[-\frac{2}{3}(\nabla \cdot \mathbf{u})\mathbf{I} + \left(\nabla \mathbf{u} + \nabla \mathbf{u}^T\right)\right]$$

represents the viscous stress tensor.

- Total Energy:

$$\frac{\partial}{\partial t}(\rho e_t) + \nabla \cdot [(\rho e_t + p)\mathbf{u}] = \nabla \cdot \left[\mathbf{q}_e + M^2(\tau \cdot \mathbf{u})\right], \tag{3}$$

where

$$\begin{aligned} e_t &= e + \frac{M^2}{2}\mathbf{u} \cdot \mathbf{u} \\ e &= \sum_{i=1}^{N} h_i Y_i - \frac{p}{\rho} \\ h_i &= h_{f_i}^{\circ} + \int_{p^\circ}^{p}\int_{T^\circ}^{T} C_{p_i}(T,p)dTdp \end{aligned}$$

represents the total internal energy, internal energy and enthalpy of the i^{th} species, respectively, and $\mathbf{q}_e$ the energy diffusion flux.

- Species:

$$\frac{\partial}{\partial t}(\rho Y_i) + \nabla \cdot (\rho Y_i \mathbf{u}) = \nabla \cdot \mathbf{q}_i + \dot{\omega}_i \qquad i = 1, \ldots, N-1, \tag{4}$$

where $\mathbf{q}_i$ and $\dot{\omega}_i$ represent the mass diffusion fluxes and the rate of production of the i^{th} species, respectively.

The viscous stress tensor is assumed to follow Stokes' hypothesis and the heat release due to chemical reaction in Eq. (3) is accounted for in the description of the specific enthalpies, h_i, as given by the enthalpy of formation, $h_{f_i}^{\circ}$. The heat release rate can be represented equivalently, as a source term on the right hand side of Eq. (3), as the product of the enthalpy of formation and the local rate of production of all the species considered in the system. Using this representation, the source term and specific enthalpies would be defined as

$$\dot{Q}_e = -\sum_{i=1}^{N} \dot{\omega}_i h_{f_i}^{\circ}, \text{ and} \tag{5}$$

$$h_i = \int_{p^\circ}^{p}\int_{T^\circ}^{T} C_{p_i}(T,p)dTdp. \tag{6}$$

Equations (1) through (4), coupled with 1) an appropriate equation of state, 2) appropriate treatments of thermodynamic and transport properties, and 3) validated mixing and combining rules for the mixtures of interest accommodate the most general system of interest including cases where multicomponent and/or preferential diffusion processes are present.

FILTERED CONSERVATION EQUATIONS. Implementation of LES and the generalized SGS closure employed are discussed in detail by Oefelein [12] and thus will be omitted here. The discussion provided in [12] includes a description of the baseline SGS model framework, implementation of the dynamic procedure, the filtering process, and issues related to the treatment of sprays, liquids and high-pressure "dense" gases. Various validation studies are also discussed to highlight the maturity of the model. Here we apply this framework to the specific case of high-pressure gaseous injection processes.

For LES applications, the filtered version of Eqs. (1)–(4) are solved. These equations are given, respectively, as:

$$\frac{\partial \overline{\rho}}{\partial t} + \nabla \cdot (\overline{\rho}\tilde{\mathbf{u}}) = 0, \tag{7}$$

$$\frac{\partial}{\partial t}(\overline{\rho}\tilde{\mathbf{u}}) + \nabla \cdot \left[\left(\overline{\rho}\tilde{\mathbf{u}} \otimes \tilde{\mathbf{u}} + \frac{\mathcal{P}}{M^2}\mathbf{I}\right)\right] = \nabla \cdot \vec{\vec{\mathcal{T}}}, \tag{8}$$

$$\begin{aligned} \frac{\partial}{\partial t}(\overline{\rho}\tilde{e}_t) &+ \nabla \cdot [(\overline{\rho}\tilde{e}_t + \mathcal{P})\tilde{\mathbf{u}}] \\ &= \nabla \cdot \left[\left(\vec{\mathcal{Q}}_e + M^2(\vec{\vec{\mathcal{T}}} \cdot \tilde{\mathbf{u}})\right)\right] + \overline{\dot{Q}}_e, \end{aligned} \tag{9}$$

$$\frac{\partial}{\partial t}(\overline{\rho}\tilde{Y}_i) + \nabla \cdot (\overline{\rho}\tilde{Y}_i\tilde{\mathbf{u}}) = \nabla \cdot \vec{\mathcal{S}}_i + \overline{\dot{\omega}}_i. \tag{10}$$

The terms $\mathcal{P}$, $\vec{\vec{\mathcal{T}}}$, $\vec{\mathcal{Q}}_e$ and $\vec{\mathcal{S}}_i$ represent respective composite (i.e., molecular plus *SGS*) stresses and fluxes. The terms $\overline{\dot{Q}}_e$ and $\overline{\dot{\omega}}_i$ represent the filtered energy and species source terms.

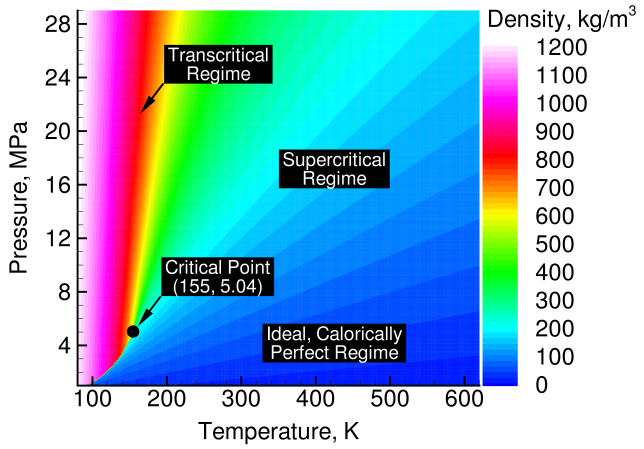

Figure 1: Thermodynamic regimes of interest using oxygen as an example.

The subgrid-scale closure is obtained using the "mixed" dynamic Smagorinsky model by combining the models proposed by Erlebacher, Hussaini, Speziale and Zang [20] and Speziale [21] with the dynamic modeling procedure [22–26]. The composite stresses and fluxes in Eqs. (7)–(10) are given as

$$\begin{aligned}\vec{\vec{\mathcal{T}}} &= (\mu_t+\mu)\frac{1}{Re}\left[-\frac{2}{3}(\nabla\cdot\tilde{\mathbf{u}})\mathbf{I}+\left(\nabla\tilde{\mathbf{u}}+\nabla\tilde{\mathbf{u}}^T\right)\right]\\ &\quad -\overline{\rho}\left(\widetilde{\tilde{\mathbf{u}}\otimes\tilde{\mathbf{u}}}-\tilde{\tilde{\mathbf{u}}}\otimes\tilde{\tilde{\mathbf{u}}}\right), \qquad (11)\end{aligned}$$

$$\begin{aligned}\vec{\mathcal{Q}}_e &= \left(\frac{\mu_t}{Pr_t}+\frac{\mu}{Pr}\right)\frac{1}{Re}\nabla\tilde{h}+\sum_{i=1}^{N}\tilde{h}_i\vec{\mathcal{S}}_i\\ &\quad -\overline{\rho}\left(\widetilde{\tilde{h}\tilde{\mathbf{u}}}-\tilde{\tilde{h}}\tilde{\tilde{\mathbf{u}}}\right), \text{ and} \qquad (12)\end{aligned}$$

$$\vec{\mathcal{S}}_i = \left(\frac{\mu_t}{Sc_{t_i}}+\frac{\mu}{Sc_i}\right)\frac{1}{Re}\nabla\tilde{Y}_i-\overline{\rho}\left(\widetilde{\tilde{Y}_i\tilde{\mathbf{u}}}-\tilde{\tilde{Y}}_i\tilde{\tilde{\mathbf{u}}}\right). \qquad (13)$$

The term μ_t represents the *SGS* eddy viscosity, given by

$$\mu_t = \overline{\rho}C_R\Delta^2\Pi_{\tilde{\mathbf{S}}}^{\frac{1}{2}}, \qquad (14)$$

where

$$\Pi_{\tilde{\mathbf{S}}} = \tilde{\mathbf{S}}:\tilde{\mathbf{S}}, \text{ and } \tilde{\mathbf{S}} = \frac{1}{2}\left(\nabla\tilde{\mathbf{u}}+\nabla\tilde{\mathbf{u}}^T\right). \qquad (15)$$

The terms C_R, Pr_t, and Sc_{t_i} represent the Smagorinsky, *SGS*-Prandtl and *SGS*-Schmidt numbers and are evaluated dynamically as functions of space and time. The overall model includes the Leonard and cross-term stresses and provides a Favre averaged generalization of the Smagorinsky eddy viscosity model [27] coupled with gradient diffusion models that simulate subgrid-scale mass and energy transport processes.

THERMODYNAMIC AND TRANSPORT PROPERTIES. Our model provides a generalized treatment of the equation of state, thermodynamics, transport processes, and chemical kinetics for any arbitray hydrocarbon mixture, including hydrogen, oxygen and nitrogen. The property evaluation scheme is designed to account for thermodynamic nonidealities and transport anomalies over a wide range of pressures and temperatures. An example of typically encountered thermodynamic regimes is shown in Fig. 1.

To account for thermodynamic non-idealities and transport anomalies over a wide range of pressures and temperatures, we apply an extended corresponding-states principle similar to that developed by Rowlinson and Watson [28] with two different equations of state. A 32-term Benedict-Webb-Rubin (*BWR*) equation of state is used to predict the pressure-volume-temperature (*PVT*) behavior of the liquid-phase, saturated vapor mixtures, and gas phase properties in the vicinity of the critical point. The Soave-Redlich-Kwong (*SRK*) equation of state [29, Chapter 3] is used elsewhere.

The law of corresponding-states expresses the generalization that equilibrium properties which depend on intermolecular forces are related to the critical properties in a universal way. In 1873, van der Waals showed that this law is theoretically valid for all pure substances whose *PVT* properties can be expressed in terms of a two-constant equation of state. In 1939, Pitzer showed that this law is similarly valid for substances which can be described by a two parameter intermolecular potential function. The corresponding-states principle holds well for fluids containing simple molecules and, upon semi-empirical extension, also holds for more complex mixtures.

The corresponding-states model used in this study is based on three assumptions: 1) the configurational properties of a single phase mixture η_m can be equated to those of a hypothetical pure fluid; i.e.,

$$\eta_m(\rho,T,X_1,\ldots,X_N) = \eta_x(\rho,T) \qquad (16)$$

2) the properties of the hypothetical pure fluid obey classical two parameter corresponding-states formalism

$$\eta_x(\rho,T) = \eta_o F_\eta(W_o,W_x,\hbar_x,f_x) \qquad (17)$$

where η_o corresponds to a reference fluid; and 3) the reference fluid density and temperature, ρ_o and T_o, obey an extended equilibrium corresponding-states principle given by

$$\rho_o = \rho\hbar_x \qquad T_o = T/f_x \qquad (18)$$

The terms $\hbar_x$, f_x and W_x in Eqs. (16)–(18) are, respectively, the equivalent substance volume reducing ratio, the equivalent substance temperature reducing ratio, and molecular weight for the multicomponent mixture. The equivalent substance volume reducing ratio accounts for the distribution of energy with respect to the reference fluid. The temperature reducing ratio accounts for molecular size differences. F_η in Eq. (17) is a dimensional scaling factor. The functional forms of these parameters are described below.

Implementation of the corresponding-states methodology requires the selection of a reference fluid. In this study methane is employed for two reasons. First, a reliable database exists with sufficient data correlated for the equation of state, relevant thermodynamic properties, and transport properties. Second, it is similar in structure to the chemical systems of interest.

To apply the model to mixtures, analytical expressions for F_η must be specified along with a set of mixing and combining rules for $\hbar_x$, f_x and W_x, a reference fluid equation of state, and relevant property data for the reference fluid. Following Leland and Chappelear[30], the mixing rules employed are as follows

$$\hbar_x = \sum_{i=1}^{N}\sum_{j=1}^{N} X_i X_j \hbar_{ij} \tag{19}$$

$$f_x = \hbar_x^{-1} \sum_{i=1}^{N}\sum_{j=1}^{N} X_i X_j f_{ij} \hbar_{ij} \tag{20}$$

$$W_x^{n/2} f_x^{1/2} \hbar_x^{-4/3} = \sum_{i=1}^{N}\sum_{j=1}^{N} X_i X_j W_{ij}^{n/2} f_{ij}^{1/2} \hbar_{ij}^{-4/3} \tag{21}$$

where subscript ij corresponds to binary pair parameters. Combining rules for these terms are given by

$$\hbar_{ij} = \frac{1}{8}\left(\hbar_i^{1/3} + \hbar_j^{1/3}\right)^3 (1 - \ell_{ij}) \tag{22}$$

$$f_{ij} = (f_i f_j)^{\frac{1}{2}} (1 - k_{ij}) \tag{23}$$

$$W_{ij} = \frac{2 W_i W_j}{W_i + W_j} \tag{24}$$

In Eqs. (22) and (23), the quantities l_{ij} and k_{ij} represent binary interaction parameters which account for molecular energy and volumetric effects in the binary system. The quantities $\hbar_i$ and f_i are the equivalent substance reducing ratios for compound i in the mixture. These quantities are obtained by a two-parameter methodology as follows

$$\hbar_i = \left(\frac{V_{c,i}}{V_{c,o}}\right) \phi_i(V_{r,i}, T_{r,i}, \omega_i) \tag{25}$$

$$f_i = \left(\frac{T_{c,i}}{T_{c,o}}\right) \theta_i(V_{r,i}, T_{r,i}, \omega_i) \tag{26}$$

Functions ϕ_i and θ_i are shape factors [31, 32] which account for non-sphericity with respect to molecular structure. Subscript c denotes a critical value, r a reduced value.

The functional form of the *BWR* equation of state is

$$p(\rho, T) = \sum_{n=1}^{9} a_n(T)\rho^n + \sum_{n=10}^{15} a_n(T)\rho^{2n-17} \exp -\gamma\rho^2 \tag{27}$$

where γ is an empirically fitted parameter termed the strain rate. Coefficients a_n are functions of temperature and the universal gas constant R_u. These quantities are given as

$$\begin{aligned}
a_1(T) &= R_u T \\
a_2(T) &= N_1 T + N_2 T^{1/2} + N_3 + N_4/T + N_5/T^2 \\
a_3(T) &= N_6 T + N_7 + N_8/T + N_9/T^2 \\
a_4(T) &= N_{10} T + N_{11} + N_{12}/T \\
a_5(T) &= N_{13} \\
a_6(T) &= N_{14}/T + N_{15}/T^2 \\
a_7(T) &= N_{16}/T \\
a_8(T) &= N_{17}/T + N_{18}/T^2 \\
a_9(T) &= N_{19}/T^2 \\
a_{10}(T) &= N_{20}/T^2 + N_{21}/T^3 \\
a_{11}(T) &= N_{22}/T^2 + N_{23}/T^4 \\
a_{12}(T) &= N_{24}/T^2 + N_{25}/T^3 \\
a_{13}(T) &= N_{26}/T^2 + N_{27}/T^4 \\
a_{14}(T) &= N_{28}/T^2 + N_{29}/T^3 \\
a_{15}(T) &= N_{30}/T^2 + N_{31}/T^3 + N_{32}/T^4
\end{aligned}$$

The *SRK* equation is of the form

$$p(\rho, T) = \frac{\rho R_u T}{1 - \rho b} - \frac{\rho^2 a}{1 + \rho b} \tag{28}$$

where

$$a = \frac{\Omega_a R_u^2 T_c^2}{p_c}\left[1 + f\omega(1 - T_r^{1/2})\right]^2 \qquad b = \frac{\Omega_b R_u T_c}{p_c}$$

and

$$f\omega = 0.48 + 1.57\omega - 0.176\omega^2$$

Here, ω represents the accentric factor and Ω_a and Ω_b are empirically derived constants. When evaluated with respect to bar, $mol/liter$, and K, these constants take on the values of 0.42748 and 0.086640, respectively.

Equation (18) coupled with Eq. (27) in the vicinity of the critical point, Eq. (28) elsewhere, and the mixing rules given by Eqs. (19)–(21) are used to obtain the *PVT* behavior for the multicomponent system considered in this study. Explicit expressions for the enthalpy, Gibbs energy, and constant pressure specific heat are required as a function of temperature and pressure. Having established an analytical representation for real mixture *PVT* behavior, these properties are obtained by means of a two step process. First, respective reference properties are transformed to those for the mixture at a given pressure using the corresponding-states methodology outlined above. The equation of state is then employed to obtain a pressure correction using departure functions of the form given by Eqs. (30)–(31) [29]. These functions describe the deviation of known reference values with respect to pressure at a given temperature and composition. They are derived by means of the Maxwell relations [33, Chapter 10].

The viscosity μ and thermal conductivity λ are obtained using the methodologies developed by Ely and Hanley [34, 35]. Equations (16)–(24) are employed with scaling factors of the form

$$\Delta H = -\int_{\infty}^{V}\left(p-\frac{RT}{V}\right)dV + T\int_{\infty}^{V}\left[\left(\frac{\partial p}{\partial V}\right)_V - \frac{R}{V}\right]dV + RT(Z-1) \quad (29)$$

$$\Delta G = -\int_{\infty}^{V}\left(p-\frac{RT}{V}\right)dV - RT\ln\left(\frac{V}{V_o}\right) + RT(Z-1) \quad (30)$$

$$\Delta C_p = T\int_{\infty}^{V}\left(\frac{\partial^2 p}{\partial T^2}\right)dV - \frac{T(\partial p/\partial V)_V^2}{(\partial p/\partial V)_T} - R \quad (31)$$

$$F_\mu = \left(\frac{W_x}{W_o}\right)^{\frac{1}{2}} f_x^{\frac{1}{2}}\hbar_x^{-\frac{2}{3}} \quad (32)$$

$$F_\lambda = \left(\frac{W_o}{W_x}\right)^{\frac{1}{2}} f_x^{\frac{1}{2}}\hbar_x^{-\frac{2}{3}} \quad (33)$$

using values of $n = 1$ and $n = -1$, respectively, in Eq. (21).

For mixtures of molecules of substantially different size; i.e., when the difference between two binary species approaches volumetric ratios on the order $V_{c,1}/V_{c,2} \sim 6$, the mean density approximation given by Eq. (16) fails. Since most thermophysical properties are determined from relatively short range forces, the properties of the larger component dominate. To correct for this effect in the prediction of mixture viscosity, Eq. (32) is used together with an Enskog correction of the form given by Ely and Hanley [34]

$$\mu = \mu_o(\rho_o, T_o)F_\mu + \Delta\mu^{ENSKOG} \quad (34)$$

This correction has been shown to improve predictions for mixtures which exhibit large size and mass differences for both dense and dilute gas states.

In a similar manner, Ely and Hanley [35] propose an expression of the form

$$\lambda = \lambda_o(\rho_o, T_o)F_\lambda + \lambda''(T) + \Delta\lambda_{crit}(\rho, T) \quad (35)$$

for thermal conductivity. The first term on the right-hand side accounts for purely collisional and transitional effects. The second term accounts for transfer of energy due to internal degrees of freedom. This term is modeled by means of a modified Eucken correlation with an empirical mixing rule for polyatomic gases [29]. The last term in Eq. (35) accounts for near critical effects.

The effective diffusion coefficient $\mathcal{D}_{im}$ for each species i is related to the binary diffusion coefficients $\mathcal{D}_{ij}$ of the mixture using the formula given by Bird [36, Chapter 16]

$$\mathcal{D}_{im,g} = \frac{(1-X_i)}{\sum_{\substack{j=1\\ j\neq i}}^{N}\left(\frac{X_j}{\mathcal{D}_{ij}}\right)} \quad (36)$$

Theory describing diffusion in binary gas mixtures at low to moderate pressures has been well developed [29]. At low pressures, these coefficients vary inversely with pressure or density and are essentially independent of composition. At high pressure, however, the product $\mathcal{D}_{ij}p$ (or $\mathcal{D}_{ij}\rho$) is no longer constant. For this situation, these products decrease with increasing pressure (or density) and are dependent on composition. Thus, binary mass diffusivities are obtained by means of a two step approach. First, low-pressure theory is employed using Chapman-Enskog theory coupled with the Lennard-Jones intermolecular potential functions. A high pressure correction is then applied using the corresponding-states methodology proposed by Takahashi [37].

A *priori* validation of the accuracy of our property evaluation procedure with available experimental data is shown in Fig. 2. The experimentally obtained density data of Vargaftik [38] is compared to density calculated using our scheme. The results are in excellent agreement with the experimental data. Figure 2 also shows the specific heat, dynamic viscosity and thermal conductivity of oxygen versus temperature over the same range of temperatures and pressures. It is important to note that the methods applied here are applicable to any arbitrary hydrocarbon mixture at typical conditions of interest in IC-engines. Several other validation studies have been performed for a variety of mixtures using the the NIST database.

NUMERICAL FORMULATION. Calculations were performed using a massively parallel flow solver designed specifically for application of LES to turbulent, chemically reacting and/or multiphase flows. It solves the fully coupled conservation equations of mass, momentum, total-energy, and species in complex geometries. The temporal integration scheme employs an all Mach number formulation using the dual-time stepping technique with generalized preconditioning. The approach is 4th order accurate in time and provides a fully-implicit solution using a fully explicit and highly-scalable multistage scheme in pseudo-time. Preconditioning is applied in the inner "pseudo-time" loop and coupled to local time-stepping techniques to minimize convective, diffusive, geometric, and source term anomalies (i.e., stiffness) in an optimal manner. This, in turn, maximizes convergence rates as the system is advanced forward in time. The formulation is A-stable, which allows one to set the physical-time step based solely on accuracy considerations. This attribute alone typically provides a 2 to 3 order of magnitude increase in the allowable integration time-step compared to other contemporary methods, especially in the incompressible, low Mach number limit.

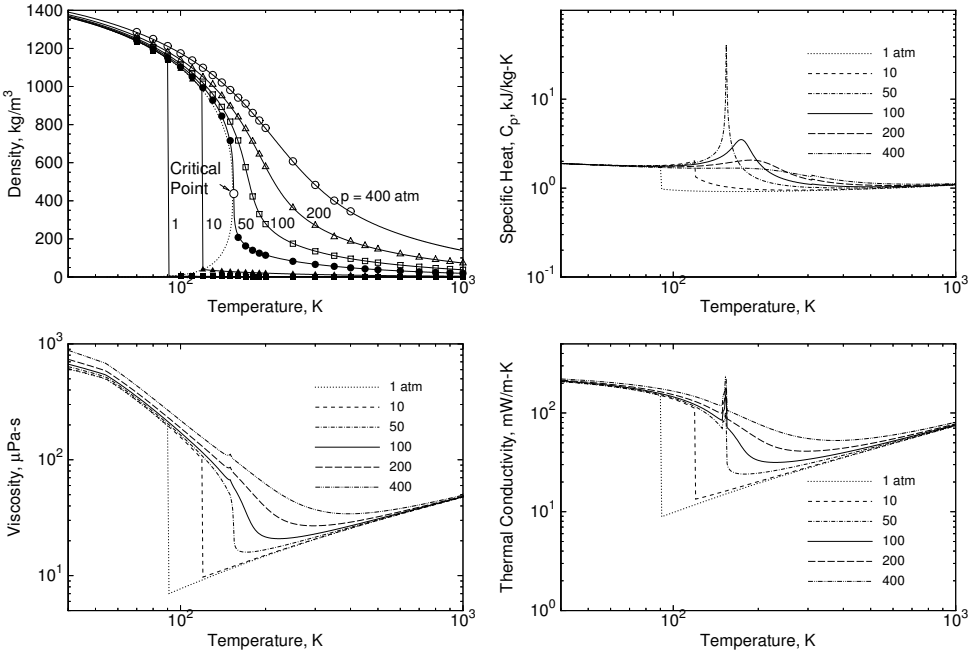

Figure 2: Density (compared with experimental data points obtained by Vargaftik [38]), specific heat, viscosity, and thermal conductivity versus temperature over the interval $40 \leq T \leq 1000$ and pressures of 1, 10, 50, 100, 200, and 400 atmospheres for pure oxygen.

The spatial scheme is designed using non-dissipative, discretely-conservative, staggered, finite-volume differencing stencils. The discretization is formulated in generalized curvilinear coordinates and employs a general R-refinement adaptive mesh (AMR) capability. This allows us to account for the inherent effects of geometry on turbulence over the full range of relevant scales while significantly reducing the total number of grid cells required in the computational domain. Treating the full range of scales is a critical requirement since turbulence-chemistry interactions are inherently coupled through a cascade of nonlinear interactions between the largest and smallest scales of the flow.

The differencing methodology has been specifically designed for LES. In particular, the 2nd order accurate staggered grid formulation, where we store scalar values at cell centers and velocity components at respective cell faces, fulfills two key accuracy requirements. First, the staggered formulation is spatially non-dissipative (i.e., possess purely imaginary Fourier characteristics), which eliminates numerical contamination of the subgrid-scale models due to artificial dissipation. Second, the stencils provide discrete conservation of mass, momentum, total energy and species, which is an imperative requirement for LES. This eliminates the artificial build up of velocity and scalar energy at the high wavenumbers, which causes both accuracy problems and numerical instabilities in turbulent flow calculations.

Table 4: Thermodynamic and transport properties for the three injection cases considered.

	H_2	N_2		
$p_0\ (MPa)$	10.4	0.101	0.336	0.722
$T_0\ (K)$	298.15	298.15	298.15	298.15
$\rho_0\ (kg/m^3)$	8.19	1.15	3.80	8.18
γ	1.43	1.40	1.40	1.42
$C_p\ (J/kg\ K)$	14600	1040	1044	1052
$\mu\ (kg/m\ s)$	8.69e-6	1.83e-5	1.83e-5	1.84e-5
$c\ (m/s)$	1381	352.1	352.4	252.8

The numerical algorithm has been designed using a fully consistent and generalized treatment for boundary conditions based on the method of characteristics. The combined formulation allows us to treat complex time-varying IC-engine geometries in a routine manner. The code has been simultaneously optimized to provide excellent parallel scalability attributes using a distributed multiblock domain decomposition with completely general connectivity. The superior scalability attributes demonstrated (both strong and weak) are a direct result of the explicit nature of the code. The algorithm is also fully vectorized and has been optimized for commodity architectures.

Table 5: Hydrogen flow conditions at the nozzle exit plane.

$P_a\ (MPa)$	0.101	0.336	0.722
$u_{avg}\ (m/s)$	255	240	236
$\dot{m}_{avg}\ (kg/s)$	6.67e-4	6.28e-4	6.19e-4

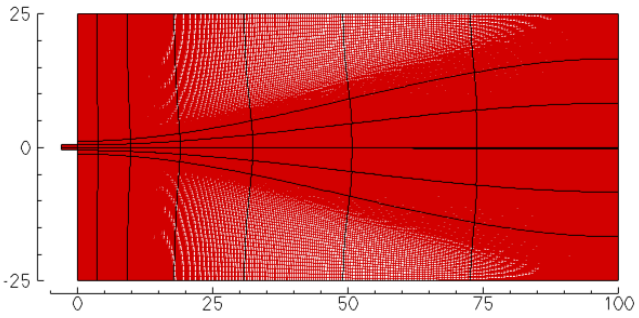

Figure 3: Cross section of the three-dimensional grid used for the calculations showing a typical multiblock decomposition.

RESULTS AND DISCUSSION

As part of our effort to validate the theoretical-numerical framework described above, we have performed a series of high-fidelity LES calculations of the three hole injector considered by Petersen and Ghandhi [18, 19]. This case represents a subset of the data provided from the experiments. Here we focus on three cases, where hydrogen is injected into nitrogen. For all three cases the hydrogen is injected at 10.4 MPa, which corresponds to Case 1 in Table 1. Chamber pressures are fixed at atmospheric, 340 kPa and 720 kPa, which corresponds to Cases 1, 2 and 3 in Table 2. The high-pressure of the injection process places it in the supercritical regime, as illustrated in Fig. 1. Key properties associated with these three cases are listed in Tables 4 and 5. Note that the orifice jet diameter in all of the calculations was 0.8 mm.

A cross-section of the curvilinear grid used for the calculations is shown in Fig. 3. The grid is stretched to provide appropriate resolution in the jet region where the shear-layer interactions are the strongest. Calculations were performed in a domain that was 100 jet diameters long and 50 jet diameters wide. The full three-dimensional grid contained 128x160x160 cells the axial (x) and transverse (y,z) directions, respectively. The injector port was also included to resolve the boundary layer, with stretching applied in the wall-normal direction such that the first cell from the wall was within a y^+ value of 1 and the first 16 cells within the interval $0 < y^+ < 30$. The grid spacing was set such that Δx^+ and Δz^+ where approximately 50. No-slip boundary conditions were applied at the upper and lower walls.

To facilitate efficient calculations, the computational domain was decomposed into 800 16x16x16 blocks, with each block run on a separate processor. A typical multiblock decomposition is shown by the black lines in Fig. 3.

Each of the cases considered is advanced in time with a time step of approximately 30 ns. The total simulation time is approximately 1 to 3 ms, depending on the case. Each case consumes approximately 50,000 to 100,000 cumulative CPU hours on a CRAY XT4 platform. In each case the maximum CFL number based on the convective velocity is limited to a value of 0.1. Injection of hydrogen into the nitrogen filled chamber is initiated by ramping the mass flow of the jet from zero to the peak value listed in Table 5 over an interval of 0.75 ms. The ramping function employed corresponds with that measured in the experiments.

A representative result is given in Fig. 4, which shows the level of qualitative agreement obtained between the experimentally observed and simulated results for the case when the chamber pressure is 0.34 MPa. On the left we show the instantaneous shadowgraph from the experiment. On the right we show instantaneous iso-contours of density from the LES solution at the same instant in time. Blue represents the density of the pure hydrogen stream (0.273 kg/m^3), red represents the density of pure nitrogen (3.80 kg/m^3) and yellow represents an intermediate value of the mixture density (2.04 kg/m^3). Similar results have been obtained for all of the cases.

Comparisons between the shadowgraph data and corresponding LES suggest that the fine-scale turbulent structure (which dominates the spatial evolution of the flow) can be reproduced quite accurately in the simulations. This is a crucial requirement for developing accurate (and cheaper) predictive models and provides us with a way to perform detailed analysis of these types of flow in a manner that is anchored to actual data. Our ongoing studies of these types of processes will include detailed analysis of the turbulent structure and the related dynamics and scalar mixing processes.

As a next step in validating our model, we have performed detailed comparisons with the jet penetration data provided from the experiments. Figures 5–7 show results correpsonding to Conditions 1, 2 and 5 in Table 2, respectively. The penetration length was calculated by measuring the distance from the jet's exit to a location along the centerline where the mass fraction of hydrogen fell below a value of 3% of the maximum. In each case the LES results are in good agreement with the experimental data. Calculations of the entire set of injectors are in progress with the objective of further detailed evaluation and analysis of more complex issues such as jet-jet interactions. In addition to direct use of the model in a companion set of in-cylinder calculations, results from these studies will be used to systematically progress toward liquid hydrocarbon fuels.

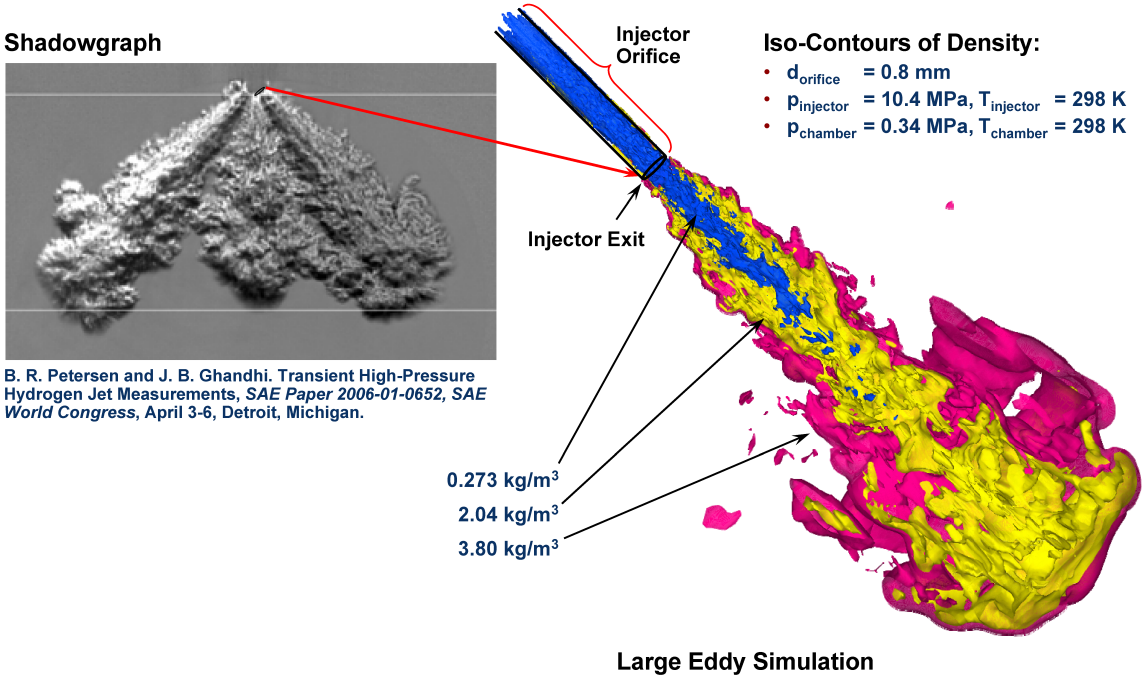

Figure 4: LES of the instantaneous jet structure compared to the corresponding shadowgraph results of Petersen *et al.* [18, 19] for Condition 2 in Table 2.

CONCLUSIONS

A series of high-fidelity Large Eddy Simulations of high-pressure hydrogen injectors have been conducted. To account for the relevant physical processes, a novel thermodynamic and transport property evaluation scheme has been developed and implemented and a baseline level of validation has been established. This scheme accounts for thermodynamic nonidealities and transport anomalies over a wide range of pressures and temperatures. In addition to the simple binary system considered here, the overall scheme is applicable to a wide variety of hydrocarbon mixtures.

The simulation results were compared to the experiments of Petersen and Ghandhi [18, 19]. Good qualitative and quantitiative agreement was obtained by comparing both shadowgraph results and the jet penetration data acquired in the experiment. The LES resolved turbulence structures are also in good qualitative agreement with those observed experimentally. The current work provides a baseline level of validation. Ongoing extensions include performing a systematic study of a variety of injector configurations with emphasis placed on development of improved engineering based models.

ACKNOWLEDGEMENTS

The authors would like to thank B. R. Petersen and J. B. Ghandhi from the University of Wisconsin, Madison, for providing the experimental data used for validation in this study. Support for this research was provided by the U.S. Department of Energy, Office of FreedomCAR and Vehicle Technologies Program. The research was performed at the Combustion Research Facility, Sandia National Laboratories, Livermore, California. Sandia is a multiprogram laboratory operated by the Sandia Corporation, a Lockheed Martin Company, for the United States Department of Energy's National Nuclear Security Administration under contract DE-AC-94AL85000.

REFERENCES

[1] F. Zhao, editor. *Homogeneous Charge Compression Ignition (HCCI) Engines: Key Research and Development Issues*. SAE International, March 2003.

[2] S. Kook, C. Bae, P. Miles, D. Choi, and L. M. Pickett. The influence of charge dilution and injection timing on low-temperature diesel combustion and emissions. In *Powertrain and Fluid Systems Conference and Exhibition*, volume 114 of *SAE Transactions*. SAE International, San Antonio, Texas, USA, October 2005. SAE Paper 2005-01-3837.

[3] L. M. Pickett. Low flame temperature limits for mixing-controlled diesel combustion. *Proc. Combust. Inst.*, 30(2):2727–2735, January 2005.

[4] L. M. Das. Hydrogen engines: A view of the past and a look into the future. *Int. J. Hydrogen Energy*, 15(6):425–443, 1990.

[5] H. Eichlseder, T. Wallner, R. Freymann, and J. Ringler. The potential of hydrogen internal com-

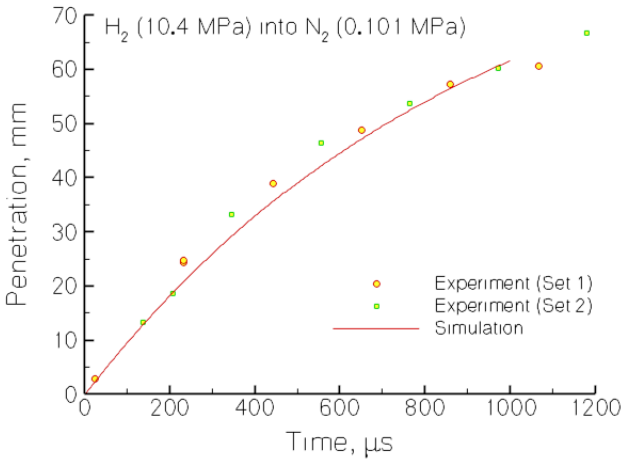

Figure 5: Jet penetration length as a function of time compared to the experimental measurements of Petersen *et al.* [18, 19] for Condition 1 in Table 2.

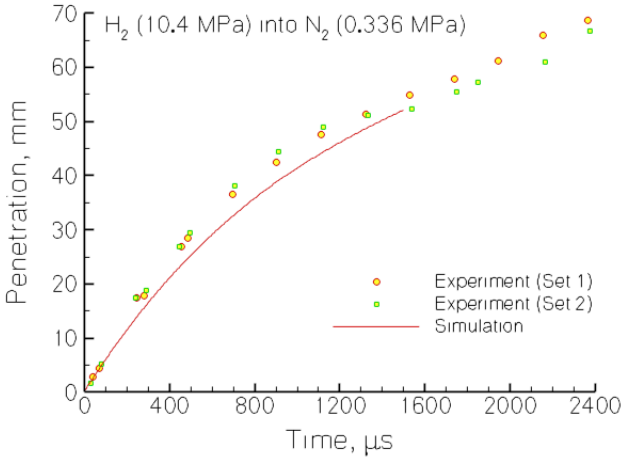

Figure 6: Jet penetration length as a function of time compared to the experimental measurements of Petersen *et al.* [18, 19] for Condition 2 in Table 2.

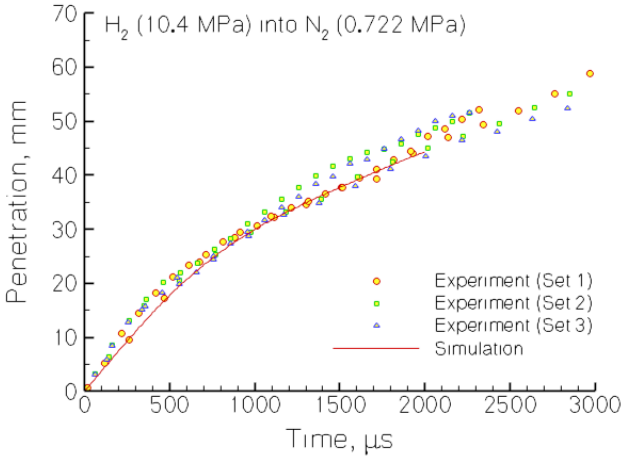

Figure 7: Jet penetration length as a function of time compared to the experimental measurements of Petersen *et al.* [18, 19] for Condition 5 in Table 2.

bustion engines ina future mobility scenario. In *Future Transportation Technology Conference*, Costa Mesa, California, USA, June 2003. SAE, SAE International.

[6] C. M. White, R. R. Steeper, and A. E. Lutz. The hydrogen-fueled internal combustion engine: A technical review. *Int. J. Hydrogen Energy*, 31(10):1292–1305, August 2006.

[7] H. S. Homan, P. C. T. de Boer, and W. J. McLean. The effect of fuel injection on NOx emissions and undesirable combustion for hydrogen-fuelled piston engines. *Int. J. Hydrogen Energy*, 8(2):131–146, 1983.

[8] M. Berckmüller, H. Rottengruber, A. Eder, N. Brehm, G. Elsässer, G. Müller-Alander, and C. Schwarz. Potentials of a charged SI-hydrogen engine. In *Powertrain and Fluid Systems Conference and Exhibition*, Pittsburgh, Pennsylvania, USA, October 2003. SAE International. SAE Paper 2003-01-3210.

[9] R. O. Fox. *Computational Models for Turbulent Reacting Flows*. Cambridge University Press, Cambridge, UK, 2003.

[10] L. C. Berselli, T. Iliescu, and W. J. Layton. *Mathematics of Large Eddy Simulation of Turbulent Flows*. Springer-Verlag, 2006.

[11] P. Sagaut. *Large Eddy Simulation of Incompressible Flows: An Introduction*. Springer-Verlag, third edition, 2006.

[12] J. C. Oefelein. Large eddy simulation of turbulent combustion processes in propulsion and power systems. *Prog. Aerosp. Sci.*, 42(1):2–37, January 2006.

[13] J. C. Oefelein, T. G. Drozda, and V. Sankaran. Large eddy simulation of turbulence-chemistry interactions in reacting flows. *J. Phys. Conf. Ser.*, 46:16–27, 2006.

[14] R. Jhavar and C. J. Rutland. Using large eddy simulations to study mixing effects in early injection diesel engine combustion. In *SAE 2006 World Congress*, Detroit, Michigan, USA, April 2006. SAE, SAE International. SAE Paper 2006-01-0871.

[15] T. Hori, J. Senda, T. Kuge, and H. G. Fujimoto. Simulation of non-evaporative and evaporative diesel spray in constant volume vessel by use of KIVALES. In *Powertrain and Fluid Systems Conference and Exhibition*, Toronto, Ontario, Canada, October 2006. SAE, SAE International. SAE Paper 2006-01-3334.

[16] T. Hori, T. Kuge, J. Senda, and H. Fujimoto. Three-dimensional analysis of diesel spray structure by use of large eddy simulation. In *JSAE Spring Conference*, Yokohama, Japan, May 2006. SAE, SAE International. SAE Paper 2006-08-0362.

[17] T. Hori, T. Kuge, J. Senda, and H. Fujimoto. Large eddy simulation of diesel spray combustion with

eddy-dissipation model and CIP method by use of KIVALES. In *SAE 2007 World Congress*, Detroit, Michigan, USA, April 2007. SAE, SAE International. SAE Paper 2007-01-0247.

[18] B. R. Petersen and J. B. Ghandhi. Transient high-pressure hydrogen jet measurements. In *Journal of Engines*, volume 115 of *SAE Transactions*. SAE International, Detroit, Michigan, USA, April 2006. SAE Paper 2006-01-0652.

[19] B. R. Petersen. Transient high-pressure hydrogen jet measurements. Master of Science in Mechanical Engineering, University of Wisconsin-Madison, 2006.

[20] G. Erlebacher, M. Y. Hussaini, C. G. Speziale, and T. A. Zang. Toward the large eddy simulation of compressible turbulent flows. *Journal of Fluid Mechanics*, 238:155–185, 1992.

[21] C. G. Speziale. Galilean invariance of subgrid-scale stress models in the large-eddy simulation of turbulence. *J. Fluid Mech.*, 156:55–62, 1985.

[22] M. Germano, U. Piomelli, P. Moin, and W. H. Cabot. A dynamic subgrid-scale eddy viscosity model. *Physics of Fluids*, 3(7):1760–1765, 1991.

[23] P. Moin. Towards large eddy and direct numerical simulations of complex turbulent flows. *Comput. Method. Appl. M.*, 87:329–334, 1991.

[24] D. K. Lilly. A proposed modification of the Germano subgrid-scale closure method. *Phys. Fluids A*, 4(3):633–634, 1992.

[25] Y. Zang, R. L. Street, and J. R. Koseff. A dynamic mixed subgrid-scale model and its application to turbulent recirculating flows. *Physics of Fluids*, 5(12):3186–3195, 1993.

[26] B. Vreman, B. Geurts, and H. Kuerten. On the formulation of the dynamic mixed subgrid-scale model. *Physics of Fluids*, 6(12):4057–4059, 1994.

[27] J. Smagorinsky. General circulation experiments with the primitive equations. I. The basic experiment. *Mon. Wea. Rev.*, 91(3):99–164, 1963.

[28] J. S. Rowlinson and I. D. Watson. The prediction of the thermodynamic properties of fluids and fluid mixtures–I. The principle of corresponding states and its extensions. *Chemical Engineering Science*, 24(8):1565–1574, 1969.

[29] R. C. Reid, J. M. Prausnitz, and B. E. Polling. *The Properties of Liquids and Gases*. McGraw-Hill, New York, New York, 4th edition, 1987.

[30] T. W. Leland and P. S. Chappelear. The corresponding states principle. A review of current theory and practice. *Industrial and Engineering Chemistry Fundamentals*, 60(7):15–43, 1968.

[31] G. D. Fisher and T. W. Leland. Corresponding states principle using shape factors. *Industrial and Engineering Chemistry Fundamentals*, 9(4):537–544, 1970.

[32] J. W. Leach, P. S. Chappelear, and T. W. Leland. Use of molecular shape factors in vapor-liquid equilibrium calculations with the corresponding states principle. *American Institute of Chemical Engineers Journal*, 14(4):568–576, 1968.

[33] G. J. VanWylen and R. E. Sonntag. *Fundamentals of Classical Thermodynamics*. John Wiley and Sons, Incorporated, New York, New York, 3rd edition, 1986.

[34] J. F. Ely and H. J. M. Hanley. Prediction of transport properties. 1. Viscosity of fluids and mixtures. *Industrial and Engineering Chemistry Fundamentals*, 20(4):323–332, 1981.

[35] J. F. Ely and H. J. M. Hanley. Prediction of transport properties. 2. Thermal conductivity of pure fluids and mixtures. *Industrial and Engineering Chemistry Fundamentals*, 22(1):90–97, 1981.

[36] R. B. Bird, W. E. Stewart, and E. N. Lightfoot. *Transport Phenomena*. John Wiley and Sons, Incorporated, New York, New York, 1960.

[37] S. Takahashi. Preparation of a generalized chart for the diffusion coefficients of gases at high pressures. *Journal of Chemical Engineering of Japan*, 7(6):417–420, 1974.

[38] N. B. Vargaftik. *Tables on the Thermophysical Properties of Liquids and Gases*. John Wiley and Sons, Incorporated, New York, New York, 2nd edition, 1975.